Chemical Science

ROYAL SOCIETY OF CHEMISTRY

EDGE ARTICLE

View Article Online
View Journal | View Issue

Cite this: *Chem. Sci.*, 2025, **16**, 15982

All publication charges for this article have been paid for by the Royal Society of Chemistry

Phosphorus-induced interfacial chemistry *via* electrolyte design for dense and highly stable potassium metal anodes†

Junpeng Xie, ‡[abf] Zhenjiang Yu, ‡[c] Jinliang Li, [b] Qing Zhang,[d] Wenjie Mai, [b] Zhixin Tai,*[a] Yajie Liu *[a] and Zaiping Guo *[e]

Potassium (K) metal anodes have attracted widespread attention in the realm of energy storage due to their cost-effectiveness, abundance, and high theoretical capacity. However, the undesirable K-dendrite growth accompanied by void formation upon prolonged cycling presents formidable obstacles to their real-world applications. Herein, phosphorus-based electrolytes are developed based on the electrolyte additive design criteria of steric hindrance, polar ability, and decomposition preference to enhance the anode/electrolyte interface stability. The additive triphenyl phosphate in the electrolyte could regulate the K^+ solvation structure and promote the formation of an inorganic P-rich solid-electrolyte interphase layer, thus ultimately mitigating interfacial polarization, augmenting transport properties, and stabilizing the interphase. Therefore, we have successfully achieved a dense and dendrite-free K metal anode, exhibiting improved coulombic efficiency and prolonged lifespan. Our design tactic demonstrates the promising application of K metal batteries in achieving elevated safety, high energy densities, and extended operational longevity.

Received 17th April 2025
Accepted 18th July 2025

DOI: 10.1039/d5sc02822a

rsc.li/chemical-science

Introduction

Rechargeable lithium (Li) ion batteries have garnered great attention due to their prevalent commercial applications, but the scarcity of Li resources and the use of flammable organic electrolytes pose insurmountable challenges for sustainable development. As an alternative solution to circumvent the inherent limitation of Li, potassium (K) ion batteries have been proposed due to the natural abundance of potassium resources, cost-effectiveness, and fascinating K^+ transport kinetics in electrolytes.[1] Moreover, the utilization of K metal as anodes, which has the lowest relative working potential (−2.93 V *vs.* SHE) and the highest theoretical specific capacity (687 mA h g^{-1}), is pivotal for fabricating high-energy-density K-ion batteries.[2] Unfortunately, the exaggerated reactivity of K metal anodes inevitably results in the formation of an unstable solid electrolyte interphase (SEI) layer, K metal voids (commonly referred to as "dead K"), and dendrite growth, particularly when they are operated in traditional organic electrolytes. This exacerbates cyclic degradation, reduces coulombic efficiency (CE), and compromises safety. So far, an enormous amount of effort has been dedicated to mitigating K metal protrusions in K metal batteries (KMBs) through interphase modification strategies, including anode recombinations,[3,4] current collector modifications,[5–7] separator decorations, and so on.[8,9] While these approaches can partially attenuate K metal protrusions, they are unable to sufficiently advance the SEI layer's cornerstone role in anode–electrolyte interface stability due to the lack of efficient and long-lasting interphase regulation.[10] The regulatory effect of salts, solvents, or additives on the solvation sheath structure of metal ions has been confirmed as a principal factor in SEI chemistry,[11] exemplified by a mixture of potassium bis(fluorosulfonyl)imide (KFSI) and potassium hexafluorophosphate, diethylene glycol di-butyl ether,[12] polydimethylsiloxane,[13] and adiponitrile.[14]

Among them, a high-concentration electrolyte (HCE) employing a suitable salt concentration (>3 M) in solvents can effectively facilitate the anion-rich solvation structure. This solvation structure, with little free solvent, usually leads to the

[a]*Advanced Energy Storage Materials and Technology Research Center, Guangdong-Hong Kong Joint Laboratory for Carbon Neutrality, Jiangmen Laboratory of Carbon Science and Technology, Jiangmen 529199, Guangdong Province, China. E-mail: liuyajie@hkustgz-jcl.ac.cn; taizhixin@hkustgz-jcl.ac.cn*

[b]*Department of Physics, Guangdong Provincial Engineering Technology Research Center of Vacuum Coating Technologies and New Materials, Jinan University, Guangzhou 510632, China*

[c]*Department of Chemistry, Lancaster University, Lancaster LA1 4YB, UK*

[d]*Shenzhen Key Laboratory of Advanced Energy Storage, Department of Mechanical and Energy Engineering, Southern University of Science and Technology, Shenzhen 518055, China*

[e]*Department of Materials Science and Engineering, City University of Hong Kong, Kowloon, Hong Kong 999077, China. E-mail: zaipiguo@cityu.edu.hk*

[f]*School of Chemistry, Guangzhou Key Laboratory of Materials for Energy Conversion and Storage, South China Normal University, Guangzhou 510006, P. R. China*

† Electronic supplementary information (ESI) available. See DOI: https://doi.org/10.1039/d5sc02822a

‡ These authors contributed equally.

formation of more contact ion pairs (CIPs) and aggregates (AGGs) compared to the dominance of separated ion pairs (SSIPs) in a normal electrolyte (NE), thereby contributing to preferential anion reduction into inorganic-rich SEI layers.[15] Considering the limitations of high viscosity, elevated cost, and sluggish kinetics in HCEs, a localized high-concentration electrolyte (LHCE) has been developed. This innovative approach involves the introduction of non-solvating diluents into HCEs to reduce salt concentration while maintaining a similar K solvation structure. For example, the addition of a diluent of 1,1,2,2,2-tetrafluoroethyl-2,2,3,3-tetrafluoropropyl ether (TTE)[16] and 1, 4-dioxane[17] in LHCE could enable a relatively durable operation of high-energy-density LMBs (over 2000 h cycling at 0.1 and 0.2 mA cm^{-2}, respectively). Unfortunately, the solvation shell in LHCEs cannot be harnessed with meticulous precision by an electrolyte additive, which is an effective factor for regulating the SEI layers. This is because the SEI layer component originates from the reported intrinsically reductive K^+-solvent complexes, which cannot support the stability of the SEI layer during charge/discharge cycling, especially at high current densities ($\geq$0.5 mA cm^{-2}), resulting in dendrite growth with uncontrolled production of "dead K" and the depletion of the electrolytes. So far, conventional additives for Li-ion batteries (fluoroethylene carbonate,[18] vinylene carbonate,[19] *etc.*) fail to regulate the interphase in the potassium storage system, and an effective electrolyte additive in the LHCE system is lacking to facilitate SEI layer stability in KMBs. Hence, in this work, novel nonflammable phosphate additives for KMBs have been developed according to the following main criteria: (1) an appropriate molecular configuration with optimal steric hindrance for regulating solvation shell participants; (2) additive solvent with strong polar groups for enhancing binding strength with K ions; (3) potential additive should possess the highest occupied molecular orbital (HOMO) and lowest unoccupied molecular orbital (LUMO) energy level for priority decomposition.

Based on our design criteria for additives above, the most appropriate additive of triphenyl phosphate (TPP) is selected from a series of phosphate additives to fabricate the electrolyte of KFSI-trimethyl phosphate (TMP)/TTE-based LHCE (M-LHCE). This TPP additive exhibits optimal steric hindrance, and greater electronegativity and SEI-forming ability than alternative additives (triethyl phosphate (TEP), tripropyl phosphate (TPrP), tributyl phosphate (TBP)), which can occupy the solvation shell of K ions, and further foster the formation of a stable P-rich and inorganic-rich SEI layer. This resulting stable electrode–electrolyte interphase mitigates interfacial overpotential, promotes ionic diffusion across the SEI layer, and thus maintains the electrode stability without dendrite formation and potassium depletion. The X-ray computed tomography (CT) techniques can also confirm the additive effect on the interphase composition and stability of the metal anode. Therefore, M-LHCE with the TPP additive could significantly extend the cycling lifespan, achieving over 550 h under a high current density (1 mA cm^{-2}, 1 mA h cm^{-2}). Our findings address the intrinsic challenges associated with metal anodes and redefine the molecular design paradigm of electrolytes for advanced KMBs in P interphase chemistry.

Results and discussion

Construction design of electrolyte molecules

The target basic electrolyte system is KFSI in TMP/TTE-based LHCE. The KFSI molecule was chosen as the salt for its good anodic compatibility[20] and pronounced nucleophilicity (5.05 eV) revealed in electrostatic potential (ESP) results *via* density functional theory (DFT) calculation (Fig. S1a†). The more uniform isosurface of TTE in ESP results also illustrates the non-nucleophilicity of the diluent function. TMP was selected as a primary solvent archetype due to its wide adaptability, inherent non-flammability, and good salt solubility.[21] However, the incompatibility between K metal and TMP-solvated molecules poses a formidable obstacle to the practical application of pure TMP-based solutions. In order to circumvent these problems, a series of phosphates was introduced as additives to weaken the interaction between cations and TMP solvent. Various additives with carbon-based functional groups, including TMP, triethyl phosphate (TEP), tripropyl phosphate (TPrP), tributyl phosphate (TBP), and TPP, were selected based on the availability of existing products, as shown in the ESP results (Fig. 1a). The distance between P and C atoms in every molecule was counted as shown in Fig. 1b, showing an increasing steric hindrance with a sequence of TMP < TEP < TPrP < TPP < TBP. It should be noted that the overlarge mean distance accompanied by excessive steric hindrance (TBP: 4.54 Å) restrains interaction between the anion and polar groups,[22] but insufficient steric hindrance (TMP: 2.64 Å, TEP:3.28 Å) results in reduced selectivity and increasing parasitic reaction.[23] TPrP (3.91 Å) and TPP (4.04 Å), which have analogous mean distances, were further distinguished by comparing the K^+-additive binding energy and polarization in Fig. 1c. This comparison indicates that TPP has the highest values in every dimension. |ESP(Max)| and |ESP(Min)| extracted from Fig. 1a indicate the ability of molecules with K-ions to change polarity and coordinate, respectively. Compared to carbon chain functional groups in others, TPP, with benzene cyclization, exhibits not only the strongest electron-withdrawing ability but also the most substantial interaction between the additive and K^+, as calculated from Table S1 and Fig. S2,† which indicates that TPP can be considered as an effective additive for solvation structure regulation.

The calculated HOMO–LUMO of these electrolyte additive molecules in Fig. 1c and S1b† can indicate their reduction, illustrating a descending trend of TBP < TPrP < TEP < TMP < TPP < KFSI. The steric hindrance is enhanced by increasing the carbon chain length in phosphate functional groups, but it impairs the capacity to form films. This hierarchy suggests that the KFSI and TPP are inclined to undergo decomposition within M-LHCE, fostering an inorganic-rich SEI layer while reducing TMP-associated parasitic reactions. The higher HOMO energy level of TPP compared to TMP underscores its prioritized reactivity of oxidation in M-LHCE, which favors the formation of protective cathode electrolyte interphase layers. Furthermore, the diluent feasibility of TTE is supported by its weakest complex interactions (Fig. S1c†) and great oxidative/reductive

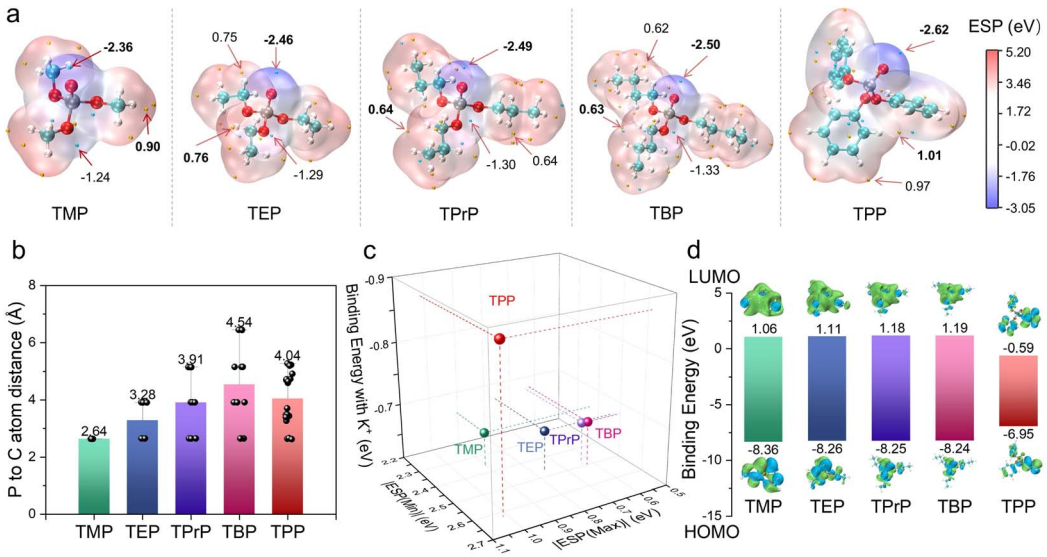

Fig. 1 Electrolyte design principle. (a) ESP mappings for a series of additive molecules. (b) Histogram of statistical distribution for the distance between P and C atoms in every additive molecule from (a). (c) Comparison of additive molecules in terms of binding energy with K^+, |ESP(Max)|, and |ESP(Min)|. (d) HOMO–LUMO energy levels for a series of additive molecules.

stability, as evidenced by HOMO–LUMO assessments. Therefore, it can be concluded that the most suitable additive of TPP can effectively serve as a partial substitute for TMP within the K^+ solvation shell. This substitution further facilitates the regulation of SEI formation through preferential decomposition, as summarized in Table 1.

Characterization of a series of electrolytes

A series of electrolytes was prepared to explore the role of the TPP additive. HCE was prepared by increasing the salt concentration to 4 M compared to the NE formulation (1.5 M KFSI-TMP). KFSI, TMP, and TTE were utilized as the foundational components (salt, solvent, and diluent, respectively) for crafting LHCE on account of the preceding analysis. The M-LHCE was obtained by incorporating the TPP additive into LHCE. Molecular dynamics (MD) simulations were conducted to investigate the solvation structures of K^+ in different aforementioned electrolytes, as shown in Fig. S3, S4†, 2a and b. The corresponding radial distribution function (RDF) confirms that TPP aligns at an identical radial distance to TMP (1.68 Å). A significant increase in TPP's coordination number, coupled with a decrease for TMP within M-LHCE compared to LHCE, indicates that TMP molecules are partially substituted by TPP in the primary K^+ solvated shells (inserted schematic diagrams in Fig. 2a and b). The inconspicuous coordination numbers for TTE confirm its minimal influence on the primary solvation architecture as an electrolyte diluent. Therefore, TPP participates in the solvation structure of K^+ within M-LHCE by ion–dipole interaction and competitive solvation dynamics, affirming its efficacy as an additive within TMP solvent-based electrolytes.

Table 1 Summary of several physical parameters shown in Fig. 1

Physical parameters	TMP	TEP	TPrP	TBP	TPP
Avg. P–C bond distance (Å)	2.64	3.28	3.91	4.54	4.04
Binding energy (eV)	−0.66	−0.67	−0.68	−0.68	−0.87
HOMO/LOMO gaps (eV)	9.42	9.37	9.43	9.43	6.36

Raman spectra of various electrolytes shown in Fig. 2c and the corresponding decoupling data in Table S2† provide evidence for the solvation structure based on our design principle. Compared to the SSIP predominant in NE, it exhibits an increased percentage of coordinated anions (CIPs + AGGs) within HCE, LHCE, and M-LHCE. TPP's integration within M-LHCE can maintain the FSI^- occupancy within the solvation shell, and TPP-induced additive-anion association amplifies the prevalence of AGGs in solvation shells to some extent, reducing the distribution of free anions in the inner Helmholtz plane, accelerating the K^+ redistribution on the electrode surface,[24] and facilitating SEI formation mainly from the additive and anion decomposition.[25] The characteristic peaks of solvents in Raman spectra are observed in Fig. S5,† and the peak shifts in different electrolytes imply the different interactions between TMP and K ions. Furthermore, Fourier transform infrared spectroscopy (FTIR) spectra in Fig. S6† also support the decreased interaction of K^+-TMP in M-LHCE. The coordination structure of ions can be further delineated using nuclear magnetic resonance (NMR) spectra as shown in Fig. 2d and S7.† The ^1H spectra show progressive downfield shifts across NE, HCE, LHCE, and M-LHCE. The pronounced shift in the M-LHCE can be attributed to the relatively weak reaction between TMP and K^+ after TPP introduction, which enhances the electronegativity of the terminal oxygen and diminishes the electron cloud density around ^1H in TMP. Additional NMR spectral evidence from regions of ^{19}F (Fig. S7a and b†) and ^{31}P

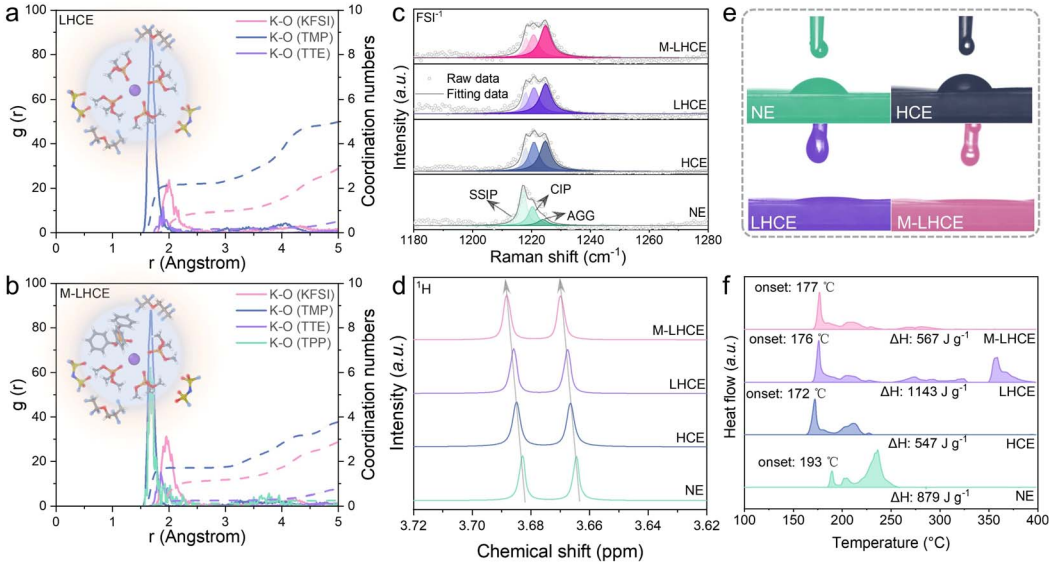

Fig. 2 Various properties for a series of electrolytes. RDFs of MD simulation in (a) LHCE and (b) M-LHCE. Inserted pictures show the corresponding solvation sheath structures. (c) The decoupling of Raman spectra for a series of electrolytes. (d) NMR spectra of ^{1}H for a series of electrolytes. (e) Contact angle test for a series of electrolytes on Cu foil. (f) DSC curves for a series of electrolytes.

(Fig. S7c†) also further substantiates the interaction-induced coordination environment of ions.

The wettability properties of electrolytes were evaluated, as shown in Fig. 2e. It demonstrates that the addition of TPP to M-LHCE can significantly enhance the interfacial contact and improve wettability, thereby promoting the mass transfer at the electrode–electrolyte interphase. The viscosity and conductivity presented in Table S3† were also in line with those trends. Furthermore, the ignition test (Fig. S8†), thermogravimetry analysis (TGA) (Fig. S9†), and differential scanning calorimetry (DSC) (Fig. 2f) also collectively verify the excellent non-flammability of M-LHCE with TPP as an additive, underscoring its safety advantages.

Interfacial chemistry and evolution

Due to the crucial role of the solvation architecture in determining interfacial composition, the TPP's solvent additive effect on the evolution of the SEI layer was investigated in this part. X-ray photoelectron spectroscopy (XPS) depth profiling was used to compare the surface components in the SEI layer after the same sputtering time in different P-dominant electrolytes (Fig. 3a, S10 and S11†). In P 2p spectra, it exhibited a pyrophosphate-like ($K_2H_4P_2O_7$) characteristic peak at a binding energy of 131.9 eV, in contrast to LHCE's phosphide-like (KP) signals at 131.5 eV, which suggests that partial substitution of TPP for TMP within the solvation shell could modulate the constituents of the phosphorus-based SEI layer.[26] The SEI layer before (Fig. S10†) and after etching (Fig. 3a) presents a relatively higher proportion distribution of C=O (inorganic), K–N, sulfide, and K–F in M-LHCE than in LHCE. This indicates that there is a complete conversion and decomposition of KFSI in M-LHCE, which can also be further verified by the corresponding anion and inorganic derivative proportion cartogram in Fig. S12† and 3b. Moreover, as seen in the C 1s XPS spectra (Fig. 3a and S13†), it shows a lower organic content (C=O and a higher value in the inorganic ingredient (CO_3^{2-}) for M-LHCE than that of LHCE, indicating that the TPP-induced SEI layer is more abundant in inorganics than in TMP solvents without the additive, thus further boosting the interface's mechanochemical robustness. The proportions of the total elements in the SEI layer composition are summarized in Fig. 3c and S14.† The much higher proportion of P 2p than C 1s, N 1s, S 2p, and F 1s reveals that P-based inorganics may dominate interfacial stability.

To explore the properties of the abundant pyrophosphate-based SEI layer in M-LHCE, electrochemical impedance spectroscopy (EIS) was further applied to investigate the SEI layer's transport behavior and surface polarization, as shown in Fig. 3d and Table S4.† It can be seen that charge transfer resistance before cycling could be significantly lessened from 8395 Ω in HCE to 4005 Ω in LHCE electrolyte, while a cell within M-LHCE exhibits the lowest resistance (3336 Ω), indicating the enhanced ionic transport in the TPP-derived interphase. Furthermore, the Nyquist plots were converted, as shown in Fig. 3e, where the Warburg factor (*i.e.*, slope) can be fitted to reflect the diffusivity in the interphase. M-LHCE (240) presents the smallest value when compared with HCE (947) and LHCE (300), illustrating the superior diffusion capability of K-ions in the SEI layer induced by TPP.[18] Given that $K_2H_4P_2O_7$-based analogs demonstrate a higher band gap (5.13 eV) than KP (0 eV) based homologous compounds (Fig. 3f and Table S5†), more excellent electrical insulation is conferred by the former. Therefore, a more favorable and stable component in the SEI layer of M-LHCE can be achieved to stabilize the interphase.

In view of K metal vulnerability under high dosage,[19] cryogenic-transmission electron microscopy (Cryo-TEM) was

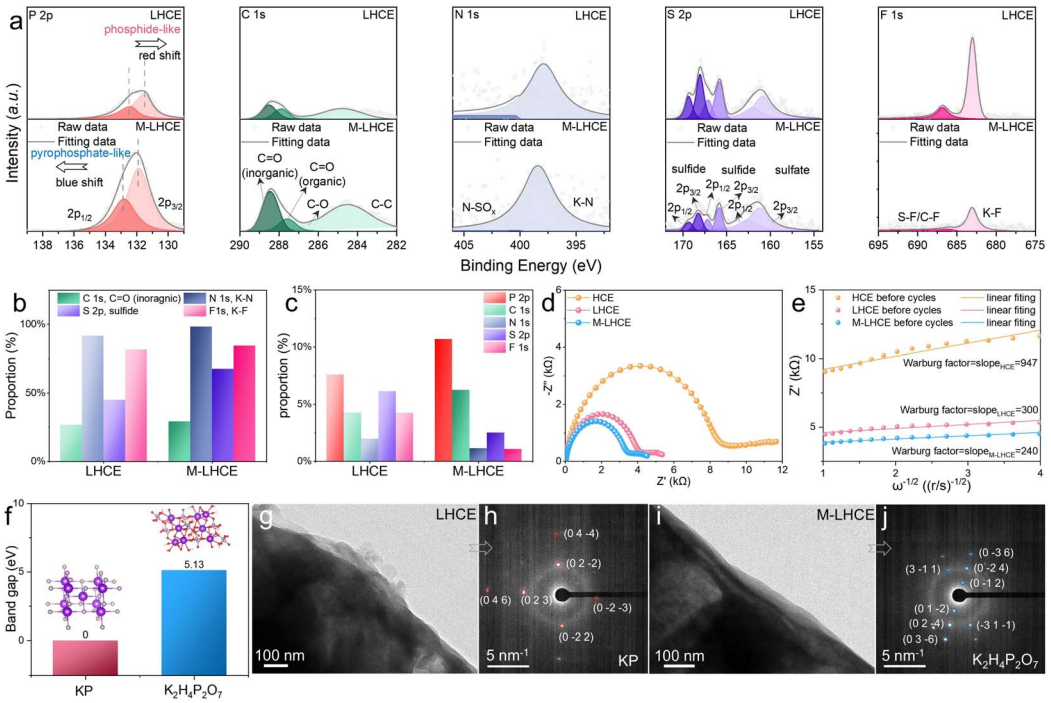

Fig. 3 Characterization of SEI layers. (a) In-depth XPS spectra of P 2p, C 1s, N 1s, S 2p, and F 1s under the same etching conditions for K metal surfaces in different electrolytes. (b) Corresponding inorganic derivative proportion cartogram in each element from (a). (c) The total element proportion in the SEI layer after etching. (d) EIS spectra for a series of electrolytes before cycling. (e) The corresponding Warburg factor in low-frequency part fitting from (d). (f) Band gap comparison between KP and $K_2H_4P_2O_7$. The inserted picture shows the corresponding structure. Cryo-TEM images of the SEI layer and the corresponding SAED images for (g) and (h) LHCE and (i) and (j) M-LHCE.

also utilized to verify the presence of phosphorus compounds. As shown in Fig. 3g and S15,† the surface of the metal in LHCE shows a coarse morphology with discernible cracks or voids formed in it. Meanwhile, M-LHCE produces a notably smoother morphology (Fig. 3i), which indicates the enhanced interfacial stability afforded by TPP derivatives. Corresponding selected area electron diffraction (SAED) images also confirm the prominent existence of KP and $K_2H_4P_2O_7$ (Fig. 3h, j, and Table S6†) within the SEI layer for LHCE and M-LHCE, respectively, aligning with XPS analysis.

Impact of the SEI layer on the morphology evolution of electrodes

The properties and ingredients of the interphase greatly influence the plating behavior and morphology of metal anodes.[27] Post-mortem scanning electron microscopy (SEM) of the K metal surface after cycling revealed that specimens are filled with voids and open holes in HCE (Fig. S16†) and LHCE (Fig. 4a), while the samples in the presence of TPP in electrolyte exhibited a smooth and hole-free appearance due to TPP-induced interfacial enhancement, as shown in Fig. 4b.

In order to further understand the interphase effect on K metal morphology in M-LHCE, we employed advanced X-ray computed tomography (CT) to visually reveal the 3D microstructure of the deposited K metal. While this technique has been used to study the morphology evolution of Li-ion battery materials,[28–30] high-resolution imaging of K metal has rarely been reported. A 3D morphological overview of the electrodeposited specimens from the surface to the bulk clearly demonstrates that the K metal deposition, using M-LHCE as the electrolyte, is denser than that in the LHCE (Fig. 4c and d). By extracting and reconstructing data from the bulk phase, moreover, the volume pore distribution image (Fig. 4e and f) further presents that the total pore volume fraction for M-LHCE (1.7%) is far less than that of LHCE (26.9%) (Fig. S17†). The deposited K metal was sliced from bottom to top, as displayed in Fig. S18† and 4g, revealing that most slices in K metal corroborate fewer or smaller voids for M-LHCE. The pore proportion, along with quantitative deposition direction, ranges within 20–30% for K metal in LHCE, which far surpasses those in M-LHCE (<1.6%). Interestingly, the pore fraction in the deposited K metal decreases along with the deposition direction for M-LHCE. However, a high void fraction remains in different cross sections after deposition in LHCE. This suppression of voids in K metal within M-LHCE likely comes from interfacial interactions between the electrolyte and K metal, and the TPP-derived SEI layer especially plays a pivotal role in mitigating void nucleation (eqn (S1)†). Moreover, the tendency for 2D horizontal void growth in K metal can be elevated in M-LHCE, as opposed to the 3D void growth observed in LHCE. This phenomenon can be attributed to the reduced interfacial energy and enhanced replenishment resulting from rapid K-ion diffusivity in M-LHCE (eqn (S2) and (S3)†).[31] Therefore, the K metal

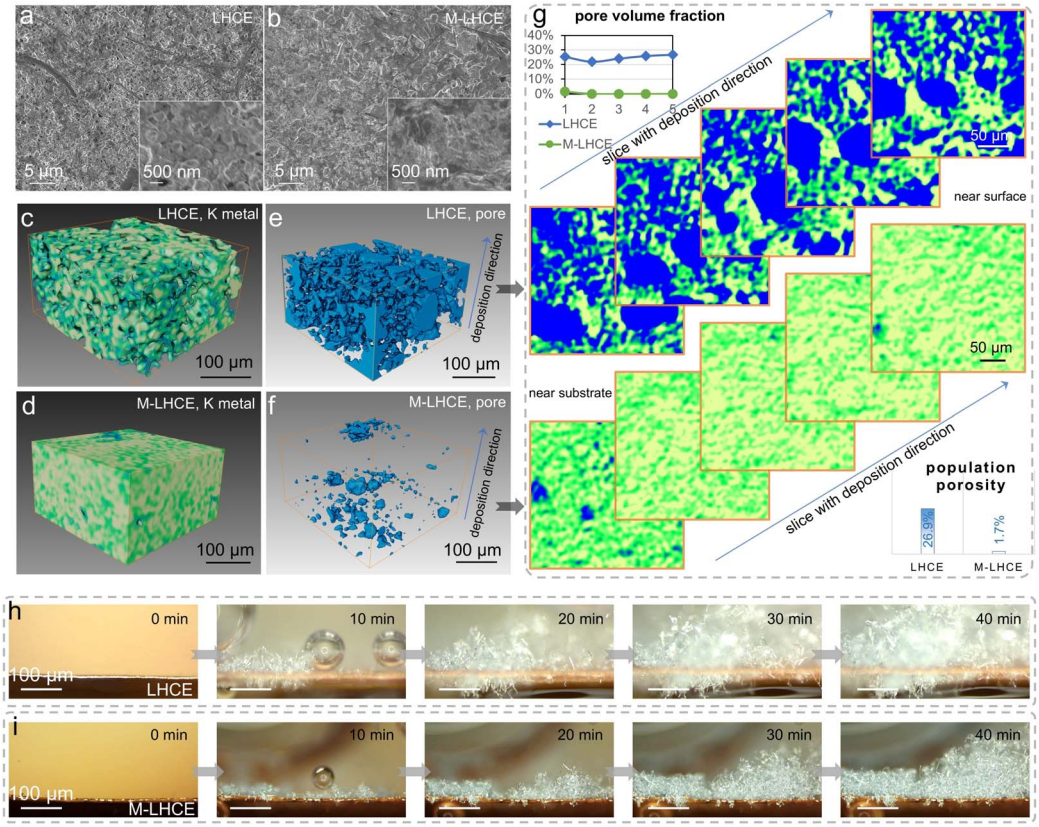

Fig. 4 The deposition behavior of K metal anodes. SEM images of K metal for (a) LHCE and (b) M-LHCE after 10 cycles. Corresponding X-ray tomography of the electrodeposited K metal in (c) LHCE and (e) M-LHCE. The distribution of the pores in (d) LHCE and (f) M-LHCE extracted from reconstructed data; (g) sliced view along with deposition direction and void quantification. The inserted ESI Table† shows the corresponding pore volume fraction and population porosity. *In situ* optical microscopy images of K metal anodes with different deposition times in electrolytes of (h) LHCE and (i) M-LHCE.

in M-LHCE exhibits fewer voids, resulting in higher K metal utilization and energy density.

In situ optical microscopy was employed to record the K metal dynamic growth process in Fig. S19†, 4h and i. It indicates that a whisker-shaped deposition of unconsolidated and uneven K metal is formed randomly on Cu foil for HCE and LHCE. In contrast, M-LHCE fosters dense and uniform nucleation and deposition of K metal on substrates from 0 to 40 min, promoting compact and 2D growth tailored by the TPP-induced SEI layer. This phenomenon, in agreement with SEM and CT results, not only curtails the growth of dendrites on K metal but also potentially improves CE.

Electrochemical performance of cells in various electrolytes

The K‖K symmetric cells were assembled to further investigate the function of the P-rich SEI layer in suppressing K penetration, as shown in Fig. S20† and 5a. Remarkably, cells employing M-LHCE exhibited an extraordinarily stable K plating–stripping behavior, enduring over 1000 hours at a current density of 0.5 mA cm^{-2} and a pulse duration of 1 h without any discernible voltage oscillations. In contrast, cells with LHCE and HCE exhibited rapid cyclic degradation, as evidenced by increased polarization or short-connection, indicating an unstable SEI layer formation. The corresponding enlarged voltage view in Fig. 5a guarantees the cycling stability of M-LHCE through successive plating–stripping processes, eliminating any possibility of misinterpretation as a short-circuit artifact.[32] This assertion was further corroborated by post-cycling separator photographs (Fig. S21†), which also provide evidence for effective dendrite suppression in the presence of M-LHCE. The other alternative additives, which have similar polarity capacity and K-ion coordination ability, deliver cycling lifetimes of 417, 473, 635, and 477 h for TMP, TEP, TPrP, and TBP, respectively (Fig. S22†). The similar steric hindrance of TPrP with TPP, as analyzed and shown in Fig. 1c, exhibits the second-best performance. This trend, verified with the steric hindrance analysis of Fig. 1b, signifies that inappropriate functional group sizes of electrolytes could impair electrochemical performance. Moreover, the symmetric cell within M-LHCE is capable of operating under even harsher cycling conditions (1 mA cm^{-2}, 1 mA h cm^{-2}) with stable operation for 550 h without any short-circuit incidents (Fig. 5b), further illustrating the superior cyclability and K metal dendrite suppression afforded by P-rich SEI layers. As shown in Fig. 5c, the corresponding nucleation and polarization overpotentials calculated from Fig. 5a also exhibit the lowest (~0.1 V) values for M-LHCE-based cells

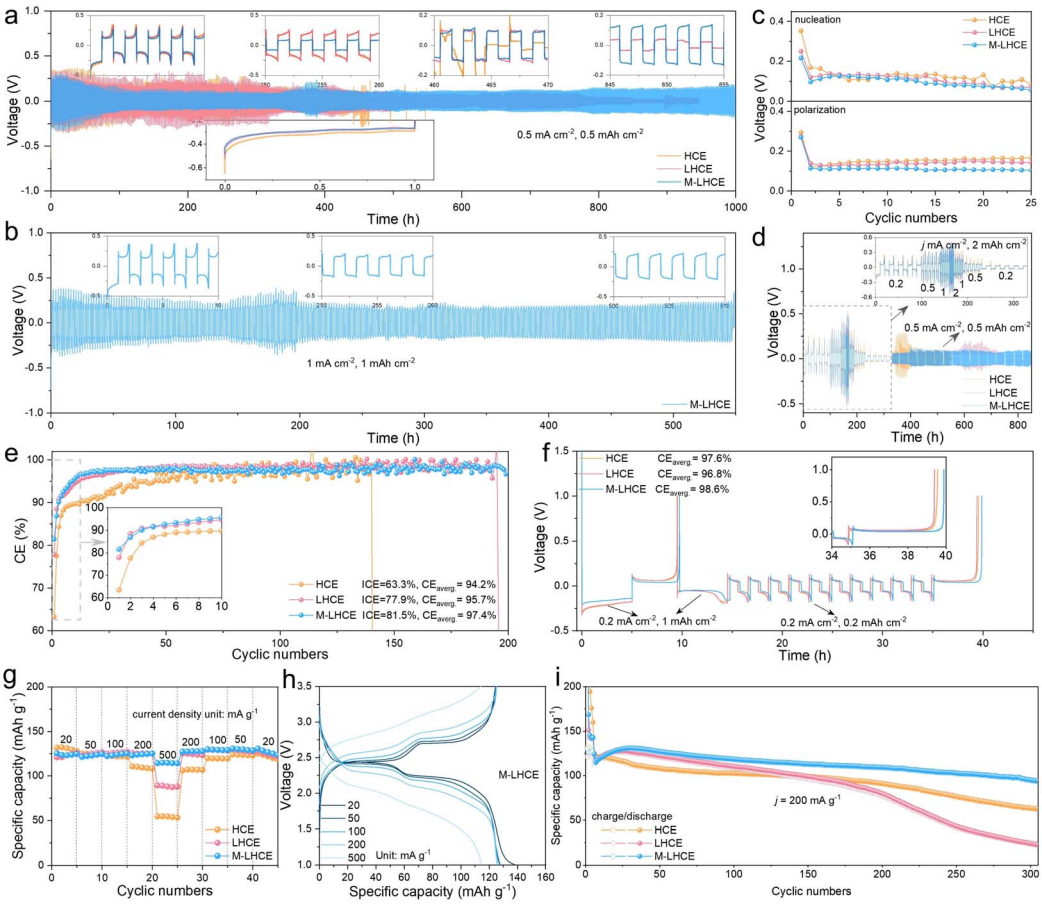

Fig. 5 Electrochemical performance of cells. (a) Voltage–time profiles of symmetric cells for a series of electrolytes cycled at 0.5 mA cm^{-2} for 1 h. (b) Voltage–time profiles for symmetric cells in LHCE cycled at 1 mA cm^{-2} for 1 h. (c) Corresponding nucleation and polarization overpotential variations calculated from (a). (d) Voltage–time profiles at different rates for symmetric cells. CE tests of a series of electrolytes by (e) conventional and (f) reservoir methods. (g) Rate performance of full cells in a series of electrolytes. (h) Corresponding GCD curves of the cell with M-LHCE in (g). (i) Long cycles of full cells in a series of electrolytes at a current density of 200 mA g^{-1}.

compared to other counterparts. It means that the TPP-prominent M-LHCE forms a stable inorganic-rich SEI layer, reducing energy barriers during the nucleation and growth of K metal.[33] We also tested the symmetric cells under different current densities ranging from 0.2 to 2.0 mA cm^{-2} while maintaining a constant area-specific capacity of 2 mA h cm^{-2} (Fig. 5d). A stable voltage profile can be achieved with M-LHCE, illustrating that high ion transport kinetics are facilitated by meticulous solvation structure regulation induced by TPP at the electrolyte–electrode interface.

The EIS spectra after cycling (Fig. S23†) confirmed this trend, indicating that the TPP-derived SEI layer can accelerate the transport of K-ions. These EIS results also agree with the wettability analysis of the contact angle test shown in Fig. 2h. Tafel plots further substantiate an enhanced exchange current density with M-LHCE (Fig. S24†), corroborating the reduced interfacial polarization and resistance. In summary, the incorporation of TPP into electrolytes can induce the SEI with high diffusion capacity and low interfacial polarization, promoting uniform and dense K deposition that dovetails with and bolsters the CT observations.

K‖Cu asymmetric cells were examined to elucidate their impact on suppressing "dead K" formation (Fig. S25†). Faster nucleation and more stable growth progress can be seen in the corresponding galvanostatic charge–discharge (GCD) curves (Fig. S26†). The initial CE (ICE) of 81.5% and the highest average CE are achieved for M-LHCE, surpassing other electrolytes, as depicted in Fig. 5e. Employing a refined reservoir method to assess average CE further confirmed these findings. It reaches an apex value of 98.6% (Fig. 5f) for M-LHCE, indicating the optimal K utilization and effective void formation within the K metal matrix. The K-ion transference numbers, as calculated in Fig.S27,† account for the rapid kinetics afforded by a higher value for M-LHCE, which is consistent with the rate performances presented in Fig. 5d. Therefore, the SEI layer derived from TPP is instrumental in promoting the formation of void-free K metal deposits. This results in superior electrochemical performance compared to other advanced electrolyte engineering approaches (Table S7†).

The full-cell performance was evaluated by using perylene-3,4,9,10-tetracarboxylic dianhydride (PTCDA) as the cathode and metal as an anode. A high-rate performance test (Fig. 5g)

demonstrates that cells with M-LHCE deliver a high specific capacity of 115 mA h g^{-1} at a current density of 500 mA g^{-1}, indicating a stark contrast to the sluggish dynamics observed with HCE at elevated current densities. The corresponding GCD curves across various current densities demonstrate the exceptional reversibility endowed by M-LHCE (Fig. S28† and 5h). As presented in Fig. 5i, the cathodes paired with M-LHCE present a long cyclability over 300 cycles and retain a high capacity of 76.1%. In contrast, those coupled with HCE and LHCE suffer from diminished specific capacity and precipitous lifecycle degradation. This fading may be attributed to the instability of the cathode–electrolyte interphase. As inferred from the XPS spectra with various electrolytes presented in Fig. S29,† this further reveals that the higher concentrations of inorganic components, such as KF and K_3N, within the SEI for M-LHCE, compared to those found in HCE and LHCE, could contribute to enhancing the stability of the cathode/electrolyte interface. A comparative analysis of the HOMO value between additives and solvents implied that additives are of great significance in stabilizing the interphase (Fig. 1d). TEM shows a thin CEI layer on the cathode after cycling within the M-LHCE electrolyte, while the surface of PTCDA cathodes in other electrolytes exhibits conspicuously thicker CEI layers (Fig. S30†). Therefore, the compact and thin inorganic-rich CEI layer derived from the TPP decomposition on the cathode–electrolyte interphase underpins the superior rate capability and long cycling stability of these cells in M-LHCE.

Conclusions

In summary, we have unveiled an ultra-stable and compressed KMB paradigm achieved through strategic electrolyte engineering design by filtering out TPP additives from nonflammable phosphorus-based candidates. The introduction of TPP in electrolytes could modify the solvation structure of K^+ and further promote the formation of a P-derived inorganic-rich SEI layer on K metal anodes. Advanced surface characterization techniques combined with electrochemical analysis reveal that the TPP-induced pyrophosphate-containing inorganic-rich SEI layer plays the prime part in protection, depolarization, and mass transport at the interphase. This design of phosphorus interphase chemistry not only prevents dendrite formation but also accelerates the formation of a dense bulk phase. Therefore, KMB anodes achieve a prolonged cycling life of 1000 h (0.5 mA cm^{-2}, 0.5 mA h cm^{-2}) and even 550 h under harsher conditions (1 mA cm^{-2}, 1 mA h cm^{-2}). At the same time, M-LHCE can also improve CE to 98.6% by suppressing "dead K" emergence. Our research paves the way for the development of next-generation dendrite-free, durable, and secure KMB, as well as other alkali-ion battery systems.

Data availability

The data supporting this article have been included as part of the ESI.†

Author contributions

J. Xie and Z. Yu performed the investigation, methodology, and data curation, and wrote the original draft. J. Li and Q. Zhang performed the investigation and characterization. W. Mai performed validation and supervision. Z. Tai, Y. Liu, and Z. Guo performed supervision and conceptualization, and wrote, reviewed and edited the final manuscript.

Conflicts of interest

There are no conflicts to declare.

Acknowledgements

This work was supported by the Guangdong Basic and Applied Basic Research Foundation (Grant No. 2023A1515110385 and 2025A1515012077), the Key Project of Basic and Applied Basic Research of Jiangmen City (Grant No. 2320002000937 and 2320002001062), China Postdoctoral Science Foundation (Grant No. 2024M751121), National Natural Science Foundation of China (No. 52401296), Guangdong S&T Programme (Grant No. 2022B1212040001) and Guangdong-Hong Kong-Macao joint Laboratory (No. 2023B1212120003). The authors thank Prof. Liang Ma from South China Normal University for the MD simulation and acknowledge the theoretical & computational assistance from Shiyanjia Lab (http://www.shiyanjia.com/).

References

1 J. Xie, J. Li, X. Li, H. Lei, W. Zhuo, X. Li, G. Hong, K. N. Hui, L. Pan and W. Mai, Ultrahigh "Relative Energy Density" and Mass Loading of Carbon Cloth Anodes for K-Ion Batteries, *CCS Chem.*, 2021, **3**, 791–799.
2 J. Xie, Y. Ji, L. Ma, Z. Wen, J. Pu, L. Wang, S. Ding, Z. Shen, Y. Liu, J. Li, W. Mai and G. Hong, Bifunctional Alloy/Solid-Electrolyte Interphase Layer for Enhanced Potassium Metal Batteries *Via* Prepassivation, *ACS Nano*, 2023, **17**, 1511–1521.
3 J. F. Wu, W. Zhou, Z. Wang, W. W. Wang, X. Lan, H. Yan, T. Shi, R. Hu, X. Cui, C. Xu, X. He, B. W. Mao, T. Zhang and J. Liu, Building K–C Anode with Ultrahigh Self-Diffusion Coefficient for Solid State Potassium Metal Batteries Operating at −20 to 120 °C, *Adv. Mater.*, 2023, **35**, e2209833.
4 W. Yuan, T. Ding, P. Mou, Y. Luo, L. Li, Y. Chen, X. Chen, J. Shu and L. Zhang, Semi-Solid CNT@NaK Anode for Potassium Metal Battery, *Adv. Funct. Mater.*, 2022, **33**, 2209774.
5 S. Li, H. Zhu, Y. Liu, Z. Han, L. Peng, S. Li, C. Yu, S. Cheng and J. Xie, Codoped porous carbon nanofibres as a potassium metal host for nonaqueous K-ion batteries, *Nat. Commun.*, 2022, **13**, 4911.
6 X. Lian, Z. Ju, L. Li, Y. Yi, J. Zhou, Z. Chen, Y. Zhao, Z. Tian, Y. Su, Z. Xue, X. Chen, Y. Ding, X. Tao and J. Sun, Dendrite-Free and High-Rate Potassium Metal Batteries Sustained by an Inorganic-Rich SEI, *Adv. Mater.*, 2024, **36**, e2306992.

7 L.-K. Zhao, X.-W. Gao, Q. Gu, X. Ge, Z. Ding, Z. Liu and W.-B. Luo, Realizing a dendrite-free metallic-potassium anode using reactive prewetting chemistry, *eScience*, 2024, **4**, 100201.
8 L. Tu, Z. Zhang, Z. Zhao, X. Xiang, B. Deng, D. Liu, D. Qu, H. Tang, J. Li and J. Liu, Polyolefin-Based Separator with Interfacial Chemistry Regulation for Robust Potassium Metal Batteries, *Angew. Chem., Int. Ed.*, 2023, **62**, e202306325.
9 P. Liu, H. Hao, H. Celio, J. Cui, M. Ren, Y. Wang, H. Dong, A. R. Chowdhury, T. Hutter, F. A. Perras, J. Nanda, J. Watt and D. Mitlin, Multifunctional Separator Allows Stable Cycling of Potassium Metal Anodes and of Potassium Metal Batteries, *Adv. Mater.*, 2022, **34**, e2105855.
10 Y. Wang, Z. Wu, F. M. Azad, Y. Zhu, L. Wang, C. J. Hawker, A. K. Whittaker, M. Forsyth and C. Zhang, Fluorination in advanced battery design, *Nat. Rev. Mater.*, 2023, **9**, 119–133.
11 Y. S. Meng, V. Srinivasan and K. Xu, Designing better electrolytes, *Science*, 2022, **378**, eabq3750.
12 Z. Yu, K. Fan, Q. Liu, D. Wang, C. Chen, Y. Zhu, H. Huang and B. Zhang, Designing Electrolytes with Steric Hindrance and Film-Forming Booster for High-Voltage Potassium Metal Batteries, *Adv. Funct. Mater.*, 2024, **34**, 2315446.
13 M. Tang, S. Dong, J. Wang, L. Cheng, Q. Zhu, Y. Li, X. Yang, L. Guo and H. Wang, Low-temperature anode-free potassium metal batteries, *Nat. Commun.*, 2023, **14**, 6006.
14 J. Park, Y. Jeong, H. Kang, T. Y. Yu, X. Xu, Y. Liu, S. Xiong, S. H. Lee, Y. K. Sun and J. Y. Hwang, A Dual-Functional Electrolyte Additive for High-Performance Potassium Metal Batteries, *Adv. Funct. Mater.*, 2023, **33**, 2304069.
15 X. Cao, H. Jia, W. Xu and J.-G. Zhang, Review—Localized High-Concentration Electrolytes for Lithium Batteries, *J. Electrochem. Soc.*, 2021, **168**, 010522.
16 P. Gao, F. Zhang, X. Wang, M. Wu, Q. Xiang, A. Yang, Y. Sun, J. Guo and Y. Huang, Ultrastable Dendrite-Free Potassium Metal Batteries Enabled by Weakly-Solvated Electrolyte, *ACS Nano*, 2023, **17**, 20325–20333.
17 J. Wen, H. Fu, D. Zhang, X. Ma, L. Wu, L. Fan, X. Yu, J. Zhou and B. Lu, Nonfluorinated Antisolvents for Ultrastable Potassium-Ion Batteries, *ACS Nano*, 2023, **17**, 16135–16146.
18 J. Xie, X. Li, H. Lai, Z. Zhao, J. Li, W. Zhang, W. Xie, Y. Liu and W. Mai, A Robust Solid Electrolyte Interphase Layer Augments the Ion Storage Capacity of Bimetallic-Sulfide-Containing Potassium-Ion Batteries, *Angew. Chem., Int. Ed.*, 2019, **58**, 14740–14747.
19 Q. Zhang, B. Han, Y. Zou, S. Shen, M. Li, X. Lu, M. Wang, Z. Guo, J. Yao, Z. Chang and M. Gu, Enabling Atomic-Scale Imaging of Sensitive Potassium Metal and Related Solid Electrolyte Interphases Using Ultralow-Dose Cryo-TEM, *Adv. Mater.*, 2021, **33**, e2102666.
20 J. Xie, J. Li, W. Zhuo and W. Mai, Recent progress of electrode materials cooperated with potassium bis(fluorosulfonyl)imide–containing electrolyte for K-ion batteries, *Mater. Today Adv.*, 2020, **6**, 100035.
21 X. Du and B. Zhang, Robust Solid Electrolyte Interphases in Localized High Concentration Electrolytes Boosting Black Phosphorus Anode for Potassium-Ion Batteries, *ACS Nano*, 2021, **15**, 16851–16860.
22 Z. Zhao, X. Zhou, B. Zhang, F. Huang, Y. Wang, Z. Ma and J. Liu, Regulating Steric Hindrance of Porous Organic Polymers in Composite Solid-State Electrolytes to Induce the Formation of LiF-Rich SEI in Li-Ion Batteries, *Angew. Chem., Int. Ed.*, 2023, **62**, e202308738.
23 K. Xu, Electrolytes and interphases in Li-ion batteries and beyond, *Chem. Rev.*, 2014, **114**, 11503–11618.
24 C. M. Efaw, Q. Wu, N. Gao, Y. Zhang, H. Zhu, K. Gering, M. F. Hurley, H. Xiong, E. Hu, X. Cao, W. Xu, J. G. Zhang, E. J. Dufek, J. Xiao, X. Q. Yang, J. Liu, Y. Qi and B. Li, Localized high-concentration electrolytes get more localized through micelle-like structures, *Nat. Mater.*, 2023, **22**, 1531–1539.
25 A. M. Li, O. Borodin, T. P. Pollard, W. Zhang, N. Zhang, S. Tan, F. Chen, C. Jayawardana, B. L. Lucht, E. Hu, X. Q. Yang and C. Wang, Methylation enables the use of fluorine-free ether electrolytes in high-voltage lithium metal batteries, *Nat. Chem.*, 2024, **16**, 922–929.
26 J. F. Moulder, W. F. Stickle, W. M. Sobol and K. D. Bomben, *Handbook of X-Ray Photoelectron Spectroscopy*, 1992.
27 J. Xie, L. Ma, J. Li, X. Yin, Z. Wen, Y. Zhong, C. Li, Y. Liu, Z. Shen, W. Mai, G. Hong and W. Zhang, Self-healing of Prussian Blue Analogues with Electrochemically Driven Morphological Rejuvenation, *Adv. Mater.*, 2022, **34**, 2205625.
28 Z. Ning, D. S. Jolly, G. Li, R. De Meyere, S. D. Pu, Y. Chen, J. Kasemchainan, J. Ihli, C. Gong, B. Liu, D. L. R. Melvin, A. Bonnin, O. Magdysyuk, P. Adamson, G. O. Hartley, C. W. Monroe, T. J. Marrow and P. G. Bruce, Visualizing plating-induced cracking in lithium-anode solid-electrolyte cells, *Nat. Mater.*, 2021, **20**, 1121–1129.
29 Z. Yu, H. Shan, Y. Zhong, X. Zhang and G. Hong, Leveraging Advanced X-ray Imaging for Sustainable Battery Design, *ACS Energy Lett.*, 2022, **7**, 3151–3176.
30 J. Li, N. Sharma, Z. Jiang, Y. Yang, F. Monaco, Z. Xu, D. Hou, D. Ratner, P. Pianetta, P. Cloetens, F. Lin, K. Zhao and Y. Liu, Dynamics of particle network in composite battery cathodes, *Science*, 2022, **376**, 517–521.
31 Y. Lu, C. Z. Zhao, J. K. Hu, S. Sun, H. Yuan, Z. H. Fu, X. Chen, J. Q. Huang, M. Ouyang and Q. Zhang, The void formation behaviors in working solid-state Li metal batteries, *Sci. Adv.*, 2022, **8**, eadd0510.
32 K.-H. Chen, K. N. Wood, E. Kazyak, W. S. LePage, A. L. Davis, A. J. Sanchez and N. P. Dasgupta, Dead lithium: mass transport effects on voltage, capacity, and failure of lithium metal anodes, *J. Mater. Chem. A*, 2017, **5**, 11671–11681.
33 A. Mohammadi, L. Monconduit, L. Stievano and R. Younesi, Measuring the Nucleation Overpotential in Lithium Metal Batteries: Never Forget the Counter Electrode!, *J. Electrochem. Soc.*, 2022, **169**, 070509.